

# Density Derivation Using Controlled Spacecraft Potential in Earth's Magnetosheath and Multi-scale Fluctuation Analysis

Daniel Teubenbacher<sup>1</sup>, Owen Roberts<sup>2</sup>, Rumi Nakamura<sup>1</sup>, Yasuhito Narita<sup>1</sup>, Zoltán Voros<sup>1</sup>, Klaus Torkar<sup>1</sup>, Per-Arne Lindqvist<sup>3</sup>, and Robert E Ergun<sup>4</sup>

<sup>1</sup>Space Research Institute, Austrian Academy of Sciences

<sup>2</sup>Space Research Institute Graz/Austrian Academy of Sciences

<sup>3</sup>KTH Royal Institute of Technology

<sup>4</sup>Univeristy of Colorado

December 7, 2022

## Abstract

In-situ measurements from the Magnetospheric Multiscale (MMS) mission are used to estimate electron density from spacecraft potential and investigate compressive turbulence in the Earth's magnetosheath. During the MMS Solar Wind Turbulence Campaign in February 2019, the four MMS spacecraft were arranged in a logarithmic line constellation enabling the study of measurements from multiple spacecraft at varying distances. We estimate the electron density from spacecraft potential for a time interval in which the ion emitters actively control the potential. The derived electron density data product has a higher temporal resolution than the plasma instruments, enabling the examination of fluctuation for scales down to the sub-ion range. The inter-spacecraft separations range from 132 km to 916 km; this corresponds to scales of 3.5 to 24.1 ion inertial lengths. The derived density and magnetic field data are used to study fluctuations in the magnetosheath through time lags on a single spacecraft and spatial lags between pairs of spacecraft over almost one decade in scale. The results show an increase in anisotropy as the scale decreases.

1                    **Density Derivation Using Controlled Spacecraft**  
2                    **Potential in Earth's Magnetosheath and Multi-scale**  
3                    **Fluctuation Analysis**

4                    **D. Teubenbacher<sup>1</sup>, O. W. Roberts<sup>1</sup>, R. Nakamura<sup>1</sup>, Y. Narita<sup>1</sup>, Z. Vörös<sup>1</sup>, K.**  
5                    **Torkar<sup>1</sup>, P.-A. Lindqvist<sup>2</sup>, R. E. Ergun<sup>3</sup>**

6                    <sup>1</sup>Space Research Institute, Austrian Academy of Sciences, Graz, Austria

7                    <sup>2</sup>Division of Space and Plasma Physics, Royal Institute of Technology, SE-100 44 Stockholm, Sweden

8                    <sup>3</sup>Laboratory for Atmospheric and Space Physics, University of Colorado, Boulder, CO 80303 USA

9                    **Key Points:**

- 10                    • High time resolution electron density is derived from spacecraft potential on MMS  
11                    during operation of the ion emitters.  
12                    • Multi-point magnetic field and the derived electron density data are used to in-  
13                    vestigate compressive turbulent fluctuations in the magnetosheath.  
14                    • The presented analysis and technique are significant for studying physical processes  
15                    in space plasmas ranging from fluid to kinetic scales.

## Abstract

In-situ measurements from the Magnetospheric Multiscale (MMS) mission are used to estimate electron density from spacecraft potential and investigate compressive turbulence in the Earth's magnetosheath. During the MMS Solar Wind Turbulence Campaign in February 2019, the four MMS spacecraft were arranged in a logarithmic line constellation enabling the study of measurements from multiple spacecraft at varying distances. We estimate the electron density from spacecraft potential for a time interval in which the ion emitters actively control the potential. The derived electron density data product has a higher temporal resolution than the plasma instruments, enabling the examination of fluctuation for scales down to the sub-ion range. The inter-spacecraft separations range from 132 km to 916 km; this corresponds to scales of 3.5 to 24.1 ion inertial lengths. The derived density and magnetic field data are used to study fluctuations in the magnetosheath through time lags on a single spacecraft and spatial lags between pairs of spacecraft over almost one decade in scale. The results show an increase in anisotropy as the scale decreases.

## 1 Introduction

Space plasmas often exhibit large-amplitude, nearly randomly-fluctuating turbulent motions. The solar wind and planetary magnetosheaths are good examples of turbulent plasmas, also showing a varying level of compressibility in terms of magnetic field magnitude and particle number density (Bruno & Carbone, 2013). As the solar wind plasma expands to the interplanetary space, instead of the expected fast adiabatic cooling, the temperature profile shows a more moderate decrease with heliospheric distance (Williams et al., 1995; Borovsky & Gary, 2014; Perrone et al., 2019). Turbulent dissipation can act through many channels such as wave-particle interactions or through dissipation in coherent structures which are intermittently distributed in space (Osman et al., 2012; Wu et al., 2013). Intermittency (Kolmogorov, 1941; Frisch, 1995; Matthaeus et al., 2015) is an indication of the existence of coherent structures, meaning structures that have longer lifetimes than the ambient stochastic fluctuations (Bruno, 2019).

In contrast to a neutral fluid, a strong magnetic field causes the turbulence to be anisotropic, with different components of the magnetic field having different powers, i.e., variance/power anisotropy (Matthaeus et al., 2005; Oughton et al., 2015). The fluctuations in a plasma become elongated along the mean magnetic field direction so that wavevectors in the perpendicular direction  $k_{\perp}$  dominate the parallel direction  $k_{\parallel}$  ( $k_{\perp} \gg k_{\parallel}$ ), i.e., there is wavevector anisotropy (Narita et al., 2011; Roberts et al., 2013, 2015). To investigate anisotropy with a single spacecraft, different intervals are investigated where the mean magnetic field direction is at different orientations with respect to the sampling direction (bulk velocity). However, this involves comparing different intervals. Ideally, to have a better understanding of kinetic scale plasma turbulence, multi-point measurements (to resolve the spatio-temporal ambiguity) with high temporal cadence (to resolve kinetic-scale fluctuations) have to be analyzed (Klein et al., 2019).

In the Earth's magnetosheath turbulence is different from the solar wind in terms of showing larger fluctuation amplitudes presumably coming from shock amplification and also a higher level of compressibility. In general, magnetosheath plasma is hotter and denser and the mean magnetic field is stronger than in the solar wind (Alexandrova (2008)). This complex process makes the magnetosheath an interesting plasma region for turbulence studies.

In February 2019, the Magnetospheric MultiScale (MMS) Solar Wind Turbulence Campaign was conducted (Burch et al., 2016; Garner, 2019; Bandyopadhyay et al., 2020; Chasapis et al., 2020). During the three-week campaign, the apogee (toward Sun) was raised to about 27  $R_E$  which enabled long intervals in the pristine solar wind, without magnetic connection to the foreshock. Additionally, the configuration of the four space-

craft was changed from a regular tetrahedron to a "logarithmic line" constellation. The inter-spacecraft distances span from about 25 to 200 km at apogee with the overall baseline being almost perpendicular to the solar wind bulk velocity direction at apogee. Having measurements from spacecraft at varying distances results in poor directional coverage as the baseline angles are almost the same for each spacecraft pairing. However, it allows the investigation of turbulent fluctuations over a larger range of spatial scales.

In this study, data from this campaign are used to study the statistical properties of (derived) electron density and magnetic field fluctuations in the Earth's magnetosheath. We first derive the electron density data from spacecraft potential measurements. During the time interval the Active Spacecraft Potential Control (ASPOC) instrument was controlling the spacecraft potential which requires a derivation scheme including the ion emitter current, the validation and statistical analysis of the electron density data. We then investigate the statistical properties of the magnetosheath plasma on the inbound portion of the orbit where the inter-spacecraft distances ranged between 132 km and 916 km to perform multi-scale analysis.

The paper is structured as follows: Section 2 presents the MMS data and describes the derivation of the electron density from spacecraft potential measurements, Section 3 shows the validation and statistical analysis of the electron density data. A discussion and summary in Section 4 concludes the paper.

## 2 MMS Spacecraft Potential as Density Estimator

The following MMS fast survey mode data are used (sampling rates in brackets) in this study: the ion current from ASPOC  $I_{ASPOC}$  (1 Hz) (Torkar et al., 2016), the spacecraft potential  $V_{sc}$  from Spin Double Probe (SDP 32 Hz) (Lindqvist et al., 2016), the electron temperature  $T_e$  and density  $n_e$  from the Fast Plasma Investigation instrument (FPI, 0.22Hz) (Pollock et al., 2016), the spin phase data from SDP (32 Hz) as well as the magnetic field data from fluxgate magnetometer FGM (16 Hz) (Russell et al., 2016). Fig. 1 shows measurements from the MMS1 spacecraft in the time period from February 26<sup>th</sup> 2019 13:00 UTC to 17:00 UTC. During this interval the ASPOC instrument was operating, resulting in a controlled spacecraft potential. The ion currents on MMS2, MMS3, and MMS4 were almost constant throughout the time window, the second ASPOC emitter on MMS1 shows a dip of the ion current for a few minutes at about 16:20 of  $\sim 14\%$  which is due to an instability in the beam.

One aim of this work was to make use of the spacecraft potential data in fast survey mode (Baker et al., 2016) at a resolution of 32 Hz to obtain electron plasma density data. In this way, the time resolution of the density data can be improved by a factor of 144 from 0.22 Hz to 32 Hz in comparison to measurements by FPI (Pollock et al. (2016)). The method used here is based on the works by Pedersen (1995), Andriopoulou et al. (2015), Torkar et al. (2015) and Nakagawa et al. (2000) and utilizes the spacecraft potential measurements and plasma moments in order to derive the electron density at high resolution. The potential calibration technique has been used for uncontrolled spacecraft potential in the past (Pedersen et al. (1984); Pedersen (1995); Pedersen et al. (2001, 2008)). Several studies also discussed the calibration when the potential was actively controlled by an ion emitter like the ASPOC instrument (Torkar et al. (2019); Andriopoulou et al. (2015); Andriopoulou et al. (2016); Andriopoulou et al. (2018)). While these reports showed some limited examples to demonstrate the method using spin-resolution data, it is the first time that this method is applied for higher-resolution data which requires some refinements removing the spin data in addition to the inclusion of the ion current from ASPOC in the derivation scheme. Furthermore, we used the derived data for analysis.

**Figure 1.** Measurements from the MMS1 spacecraft on February 26th, 2019 from 13:00 UTC to 17:00 UTC. The panels, from top to bottom represent: Electric field and magnetic field in GSE coordinates (Fränz & Harper, 2002), an omnidirectional electron energy spectrum, spacecraft potential, ASPOC ion current, electron temperature, number density of electrons and ions.

116 In the uncontrolled case, the current balance equation of a spacecraft in a tenuous  
 117 plasma is governed by the thermal electron current collected by the spacecraft  $I_e$  and  
 118 the photoelectron current  $I_{\text{phot}}$  leaving the spacecraft. The ASPOC instruments can be  
 119 used to prevent spacecraft charging greater than +4 V by emitting ions to give a cur-  
 120 rent  $I_{\text{ASPOC}}$ . Other currents can contribute to the current balance but, in general, are  
 121 much smaller (Torkar et al., 2019). The secondary electron emission is not always small.  
 122 It depends on surface material properties as well as incident electron energy. For most  
 123 materials, the peak of secondary electron emission is at around 300 - 800 eV, meaning  
 124 that if the incident electron current has a temperature outside this range, the number  
 125 of secondary electrons emitted is low (Balcon et al., 2011), which is the case for this study.  
 126 Accordingly, the following balance equation can be used when ASPOC controls the space-  
 127 craft potential:

$$I_e + I_{\text{phot}} + I_{\text{ASPOC}} = 0 \quad (1)$$

128 Assuming a Maxwellian distribution of the particle velocities, the thermal electron  
 129 current  $I_e$  (Mott-Smith & Langmuir, 1926) can be expressed as

$$I_e = -A_{\text{sc}}|q|n_e\sqrt{\frac{k_{\text{B}}T_e}{2m_e\pi}}c \quad (2)$$

130 where  $T_e$  is the electron temperature,  $q$  is the electron charge,  $m_e$  is the electron  
 131 mass,  $n_e$  is the electron density,  $k_{\text{B}}$  Boltzmann's constant and  $c = (1 + (qV_{\text{sc}}/k_{\text{B}}T_e))$   
 132 a correction factor that accounts for the surplus of electrons that is attracted due to a  
 133 positively charged spacecraft (Torkar et al., 2019).  $V_{\text{sc}}$  is the spacecraft potential and  
 134  $A_{\text{sc}} = 34 \text{ m}^2$  is the effective surface area of the MMS spacecraft.

135 If the energy of the incoming solar radiation and exact surface material properties  
 136 are known, the photoelectron current that is leaving the spacecraft can be calculated.  
 137 In addition, the area of the sunlit part of the spacecraft has to be known at every point  
 138 of time, which is especially difficult for a spinning spacecraft (Pedersen, 1995). Conse-  
 139 quently, another method to determine  $I_{\text{phot}}$  is used here. It employs the simplified cur-  
 140 rent balance equation (Eq. 1) and the floating spacecraft potential, which is established  
 141 where the current balance is given. The photoelectron current is modeled using a com-  
 142 bination of one or more exponential terms, each having a current and a potential coef-  
 143 ficient (Pedersen, 1995; Torkar et al., 2019; Andriopoulou et al., 2015). The number of  
 144 exponential terms depends on the number of photoelectron populations. In previous stud-  
 145 ies, the usage of two (Torkar et al., 2019; Nakamura et al., 2017) or three (Andriopoulou  
 146 et al., 2015) exponential terms has proven to be sufficient. In this work, the approxima-  
 147 tion with two exponential functions was used as there is one photoelectron population  
 148 with a higher current at lower energy and the other population with a lower current at  
 149 a higher energy. The model function can be written as:

$$I_{\text{phot}} = I_{01}e^{-V_{\text{sc}}/V_{01}} + I_{02}e^{-V_{\text{sc}}/V_{02}} \quad (3)$$

150 with  $I_{01}$  and  $I_{02}$  as current coefficients (current units) and  $V_{01}$  and  $V_{02}$  as potential co-  
 151 efficients (potential units) related to the characteristic energy of the respective photo-  
 152 electron population (Andriopoulou et al., 2016).

153 For using data with a time resolution higher than the spin period, 20 s (0.05 Hz),  
 154 the effect from the spin needs to be removed since the spacecraft rotation causes a con-  
 155 stant change in the sunlit area and the photoelectron emission and creates a variation  
 156 in spacecraft potential data not due to the change in the ambient electrons. The spin  
 157 effect can be seen as spikes in the Fourier spectra of the potential measurements (Yao  
 158 et al., 2011; Roberts et al., 2017). To remove the spin effect, the spin phase data along  
 159 with the spacecraft potential fluctuations are used to develop an empirical spin model  
 160 for each of the four MMS spacecraft (Roberts et al., 2017) (Roberts et al., 2020). Us-  
 161 ing a non-linear least-squares fit (Markwardt, 2009) with ten sine curves, the spin effect

162 of each spacecraft can be subtracted from the spacecraft potential data, leading to a spin-  
 163 tone removed  $V_{sc}$  that is used to derive the average photoelectron curve as well as the  
 164 electron density.

165 With the spin tone removed spacecraft potential data  $V_{sc}$  and the ASPOC ion cur-  
 166 rent  $I_{ASPOC}$ , there is only one parameter missing to derive an average photoelectron curve  
 167 in the simplified current balance model (Eq. 1). It is the thermal electron current  $I_e$ , and  
 168 it can be calculated using FPI measurements (see Eq. 2). All data are re-sampled to 4.5  
 169 s cadence, which is the time resolution of fast mode data of the FPI measurements. The  
 170 photoelectron current  $I_{phot} = I_e + I_{ASPOC}$  can be plotted against the spacecraft po-  
 171 tential, see Fig. 2. In this figure, the data points (grey dots) are binned into 100 equally  
 172 spaced potential bins, and the mean value of data points within each bin is then displayed  
 173 as a black star. The error bars represent the standard deviations of the mean bin val-  
 174 ues to the rest of the data points in each bin. The model function with two exponen-  
 175 tial functions (Eq. 3) is fitted to the data (green curve). This model function is the av-  
 176 erage photoelectron curve needed to derive electron densities from spacecraft potential  
 177 data as in Eq. (4).

178 When looking at the data points in Fig. 2, one can see that there are two “clouds”,  
 179 one between 2.5 V and 3.0 V and the second one between 4.0 V and 4.8 V. Looking at  
 180 those potential ranges in Fig. 1, it can be seen that cloud 2 corresponds to the time in-  
 181 terval between 13:00 UTC and 14:00 UTC where electron temperatures were two mag-  
 182 nitudes higher than in the time after 14:00 UTC, which can be identified as cloud 1. The  
 183 region of interest for further analysis is the time period in the magnetosheath (14:20 to  
 184 17:00 UTC), and therefore, electron temperatures are averaged over this period to  $T_{e,avg} =$   
 185  $33 eV$ . In order to derive the electron density at 32 Hz, the ASPOC ion current is in-  
 186 terpolated using cubic splines to match the data rate. This is reasonable as the ASPOC  
 187 current only shows variations of about 1 %.

188 Finally, by rearranging the current balance equation Eq. (1), the thermal electron  
 189 current (Eq. 2) and the modeled photoelectron current, the electron density can explicitly  
 190 be estimated as follows:

$$n_e = \frac{1}{A_{sc}|q|} \sqrt{\frac{2\pi m_e}{kT_e}} \frac{1}{1 + \frac{qV_{sc}}{k_B T_e}} \cdot \left[ \left( I_{01} e^{-V_{sc}/V_{01}} + I_{02} e^{-V_{sc}/V_{02}} \right) + I_{ASPOC} \right] \quad (4)$$

191 where  $n_e$  is the derived electron density,  $V_{sc}$  is the spacecraft potential and  $A_{sc} = 34 m^2$   
 192 is the effective spacecraft surface area.

193 A direct comparison of the measured and derived electron densities is shown in Fig.  
 194 3. The panel in the middle shows the normalized difference  $Err(n_e) = (n_{e,der} - n_{e,meas}) / n_{e,meas}$   
 195 between the two densities. In the time before 14:20,  $Err(n_e)$  is mostly above 100%; this  
 196 is due to the assumption made about the electron temperature. In general, one can see  
 197 that  $Err(n_e)$  and also its variation is high ( $\pm 40\%$ ) in the time period from 13:50 UTC  
 198 to 14:10 UTC. These variations might be caused by to stronger electric fields (see Fig.  
 199 1 panel 1) and thereby caused perturbations in the spacecraft potential due to enhanced  
 200 photoelectron emission when the electric field distorts the potential in the sheath around  
 201 the spacecraft. The influence of strong ambient electric fields on spacecraft potential mea-  
 202 surements was shown by Torkar et al. (2017); Graham et al. (2018); Roberts et al. (2020).  
 203 The focus of the further analysis is on the time interval after the transition into the mag-  
 204 netosheath region, where the electric field strength components are rather small ( $< 4 mV/m$ ).  
 205 In the time period from 14:10 - 17:00, the normalized difference decreases to a small value,  
 206  $Err(n_e) = -5\%$  on average.

207 The electron densities derived from the other three MMS spacecraft show quali-  
 208 tatively the same results. For MMS4, several assumptions had to be made due to the  
 209 lack of electron plasma data from FPI. First of all, the electron temperature of MMS1

**Figure 2.** MMS1 average photoelectron curve: grey dots represent data points, black stars the mean of those data points within 100 equally spaced potential bins (with standard deviations as error bars) and the green graph is the two exponential model fit for the photoelectron curve with the four coefficients written in green.

210 was used to compute the average photoelectron curve. The average  $T_e = 33$  eV is then  
 211 used for calculation. Secondly, the ion density measurement from MMS4 was used in-  
 212 stead of the electron density. The use of ion density is reasonable, and the estimation  
 213 compares well (of the order of a few percent) with the three other spacecraft.

### 214 **3 Validation of the Electron Density Data and Application to Turbu-** 215 **lence Analysis**

216 The derived density data will be validated using the - lower resolution - FPI data  
 217 sets as a comparison. We then analyze characteristics of fluctuations in both the mag-  
 218 netic field and in electron density and compare by performing statistical analysis. As the  
 219 electron density is a scalar we do not need to consider a coordinate system. However,  
 220 for the magnetic field a physically relevant coordinate system should be considered for  
 221 the comparison. We perform a coordinate transform based on the mean magnetic field  
 222 direction. The measured data are available in the geocentric solar ecliptic (GSE) coor-  
 223 dinate system, and are transformed into a parallel and two arbitrarily chosen perpen-  
 224 dicular magnetic field components:

$$225 \quad \vec{B}_{parallel}(t) = B_x(t) \cdot B_{0,x} + B_y(t) \cdot B_{0,y} + B_z(t) \cdot B_{0,z} \quad (5)$$

$$226 \quad \vec{B}_{perp1}(t) = B_x(t) \cdot e_{\perp 1,x} + B_y(t) \cdot e_{\perp 1,y} + B_z(t) \cdot e_{\perp 1,z} \quad (6)$$

$$227 \quad \vec{B}_{perp2}(t) = B_x(t) \cdot e_{\perp 2,x} + B_y(t) \cdot e_{\perp 2,y} + B_z(t) \cdot e_{\perp 2,z} \quad (7)$$

228 where  $\hat{B}_0$  is the mean magnetic field direction unit vector,  $\vec{B}_{parallel}$  points in the mean  
 229 field direction and  $\vec{B}_{\perp 1}$  and  $\vec{B}_{\perp 2}$  are the two perpendicular directions in the coordinate  
 230 system.  $\hat{e}_{\perp 1} = \hat{B}_0 \times (1, 0, 0)$  is the first perpendicular vector and the second one is  
 $\hat{e}_{\perp 2} = \frac{\hat{B}_0 \times \hat{e}_{\perp 1}}{|\hat{B}_0 \times \hat{e}_{\perp 1}|}$ .

231 This coordinate transform can be justified as if the magnetic field direction is rel-  
 232 atively stable in chosen time interval (see Fig. 3). The parallel magnetic field compo-  
 233 nent represents the compressive component and can qualitatively be compared to the  
 234 density fluctuations. Similar work was done in Roberts et al. (2022) where it is also dis-  
 235 cussed why the definition of a mean magnetic field is a sensitive issue (Oughton & Matthaeus,  
 236 2020).

237 In order to validate the potential calibration, a smaller sub-interval was selected  
 238 that complies with the following two requirements:

- 239 1. The difference of measured and derived electron densities is below 5 % on aver-  
 240 age.
- 241 2. The statistical analysis of the magnetic field will be performed in global mean mag-  
 242 netic field coordinates, therefore the direction of the magnetic field should not vary  
 243 more than 5° in the interval so that a mean magnetic field direction is well defined.

244 The challenge is to find a period that fulfils both requirements while being as long  
 245 as possible at the same time. The shorter the time series is, the greater the uncertainty  
 246 will be in determining structure functions (e.g. Dudok de Wit et al. (2013)) especially  
 247 at higher orders, or large scales. The following figure, Fig. 3 shows both, the compar-  
 248 ison of the derived and measured (FPI) electron density as well as the magnetic field mea-  
 249 surements (FGM, Russell et al. (2016)) of the MMS1 probe for the whole time interval  
 250 from 13:00 to 17:00 on February 26<sup>th</sup> 2019. When looking only at the magnetosheath  
 251 period from about 14:20 to 17:00 UTC, the longest time period where the magnetic field  
 252 does not change its direction substantially, is between 15:00 UTC and 15:40 UTC. The  
 253 average relative difference between measured and derived electron density is with -3%  
 254 relatively small. We therefore used data from this time period (15:00 UTC to 15:40 UTC)  
 255 for further analysis.

256 We investigate the statistical properties of the fluctuations using the following two  
 257 methods. The first method calculates fluctuations from a variable (magnetic field or elec-  
 258 tron density in our case) using time lags and data from only one spacecraft (Eq. 8).

$$\Delta B_{t,\tau} = B(t + \tau) - B(t) \quad (8)$$

259 The scale of the fluctuations is defined by the timescale  $\tau$ . The second method uses  
 260 different combinations of two spacecraft; a fluctuation is defined with a spatial lag as seen  
 261 in Eq. 9.

$$\Delta B_{a,b}(t) = B_a(t) - B_b(t) \quad (9)$$

262 A time lag can be converted to a spatial distance along the flow direction using the  
 263 ion bulk speed, i.e., Taylor's frozen-in flow hypothesis (Taylor, 1938). This approxima-  
 264 tion assumes that the fluctuation evolves slowly compared to the time taken for it to ad-  
 265 vect over the measurement point. The conversion of a time lag in this manner allows spa-  
 266 tial lags in different directions (along the bulk flow and along the spacecraft separation  
 267 direction) to be calculated. The novel spacecraft formation allows the comparison of tem-  
 268 poral and spatial lags over a larger range of scales than possible with a tetrahedron (e.g.,  
 269 Chhiber et al. (2018) and Chasapis et al. (2017)).

270 To quantify the power of the fluctuations in different directions we calculate the  
 271 second order structure functions (p=2) which are generally defined in Eq. 10.

$$D^{(p)} \equiv \langle |\Delta B|^p \rangle \quad (10)$$

272 Where  $\Delta B$  is calculated from time lags e.g. Eq 8 or spatial lags Eq 12 and the an-  
 273 gled brackets denote an average. Higher orders of structure functions can give insight  
 274 into properties such as the intermittency. However, we focus here on the second order  
 275 structure function, as higher orders are more susceptible to outliers especially during shorter  
 276 time intervals e.g. (K. Kiyani et al., 2006)

277 When using single spacecraft time lagged measurements; the second order struc-  
 278 ture function at a time  $\tau$  is defined as;

$$D^{(p)}(\tau) \equiv \langle |\Delta B_\tau|^p \rangle \quad (11)$$

279 Time lags can be converted to a spatial lag along the stream direction assuming  
 280 Taylor's hypothesis  $\tau = \lambda/v_b$ , with  $v_b$  being the mean ion bulk speed and  $\lambda$  being the  
 281 spatial lag. If there are measurements available from multiple satellites available such  
 282 as with MMS, it is also possible to look at the spatial variation of a measurement directly  
 283 by comparing measurements at the same times at different spatial locations. If they are  
 284 in the bulk flow direction, comparing single spacecraft time lagged variations with multi-  
 285 spacecraft spatial lag variations using the solar wind speed as proportionality factor, the  
 286 validity of Taylor's hypothesis can be evaluated (Bruno & Carbone, 2013).

287 In the multi-spacecraft case, the increments are defined as the difference between  
 288 the measurements of two spacecraft  $a, b$  at the same time  $t$ . The structure function can  
 289 then be calculated as:

$$D_{ab}^{(p)}(\lambda) \equiv \langle |(B_a(t) - B_b(t))|^p \rangle \quad (12)$$

290 Time lagged structure functions, where the timescale is converted to a spatial scale  
 291 can then be compared directly to the spatially lagged measurements.

**Figure 3.** MMS1 Multipanel Plot from 26-02-2019. The panels, from top to bottom represent: number density of electrons measured from FPI (red) and derived with the spacecraft potential (black), and the relative difference between the measured and derived electron densities and the magnetic field measurements from FGM in GSE coordinates. The grey area marks the selected time interval for statistical analysis.

292 In the chosen time period from 15:00-15:40 UTC, the minimum separation between  
 293 two MMS spacecraft is 132 km (MMS1-MMS4) and the maximum distance is 916 km  
 294 (MMS2-MMS3). The average magnetic field strength  $\langle B \rangle$  is 13.7 nT and the root-mean-  
 295 square magnetic fluctuation weighted by the average magnetic field is  $\delta B / \langle \vec{B} \rangle = \sqrt{\langle |\vec{B}(t) - \langle \vec{B} \rangle|^2 \rangle} / \langle \vec{B} \rangle =$   
 296  $0.377$ . The average electron plasma density  $\langle n_e \rangle$  is  $35 \text{ cm}^{-3}$  and the ion and electron in-  
 297 ertial lengths are  $d_i = 38 \text{ km}$  and  $d_e = 1 \text{ km}$ . The ion plasma beta that describes the  
 298 ratio of thermal to magnetic pressure is  $\beta_i = \frac{nk_B T_i}{B^2/2\mu_0} = 10$ . Finally, the mean Alfvén  
 299 speed is  $v_A = 50 \text{ km/s}$  and the mean flow speed  $v_B = 138 \text{ km/s}$ .

300 The mean magnetic field direction during the selected time interval can be calcu-  
 301 lated by averaging the components  $\vec{B}_{mean} = [\langle B_x(t) \rangle, \langle B_y(t) \rangle, \langle B_z(t) \rangle]$ . Normalizing  
 302 leads to the unit vector  $\hat{\vec{B}}_0 = (0.14, -0.17, -0.97)$ . It can be seen that the magnetic  
 303 field mostly points in the negative z-direction, this is illustrated in Fig. 4, together with  
 304 the mean flow direction and the spacecraft positions in the XY-, XZ- and YZ-plane. One  
 305 perpendicular direction can be found as cross product of the mean field direction  $\hat{\vec{B}}_0$  with  
 306 the unit vector in X-direction, the second perpendicular direction is then the cross prod-  
 307 uct of  $\hat{\vec{B}}_0$  with the first perpendicular direction. The angle between mean magnetic field  
 308 direction and mean flow direction is  $111^\circ$  and the angle between the mean magnetic field  
 309 direction and the respective spacecraft baselines is  $85^\circ$ . It can be seen that the space-  
 310 craft baselines are parallel and measure almost perpendicular to the mean magnetic field.  
 311 The (common) baseline direction is also the movement direction of the satellites on their  
 312 orbit in this logarithmic line constellation.

313 The statistical analysis can now be performed for both, the derived electron den-  
 314 sity as well as on the magnetic field measurement in mean field coordinates. The small-  
 315 est time lag used is the time interval between two consecutive measurements, which is  
 316  $\tau_{mag,min} = 0.063 \text{ sec}$  for the magnetic field measurements as the time resolution of the  
 317 FGM instrument is 16 Hz in fast survey mode. For the electron density, the smallest time  
 318 lag is  $\tau_{den,min} = 0.032 \text{ sec}$  corresponding to 32 Hz. The largest time lag is chosen to  
 319 be  $\tau_{max} = 100 \text{ sec}$ , which is about 45% of the whole 40-min time interval. Using Eq.  
 320 10 and 12, one can compute the structure functions of order  $p = 2$  of the individual mag-  
 321 netic field components as well as the electron density as function of time lag  $\tau$ . While  
 322 the structure functions can be plotted directly, another way of analyzing the second-order  
 323 structure function implies the so-called *equivalent spectrum*  $S^{(2)} \equiv D^{(2)}\lambda$ . Together with  
 324 the effective wave number  $k^* \equiv 1/\lambda$ ,  $S^{(2)}$  shows a similar behavior as a Fourier spec-  
 325 trum and can therefore be used to estimate spectral slopes (see e.g. Chhiber et al. (2018))

326 In Fig. 5, panel (a) the equivalent spectrum for the magnetic field is shown. The  
 327 time-lagged structure functions are indicated by the solid lines, with the dotted lines rep-  
 328 resenting the parallel and perpendicular magnetic field components and the solid black  
 329 line is the so called trace magnetic field structure function. At large scales, the equiv-  
 330 alent spectrum of the magnetic field follows the  $1/f$  regime (K. H. Kiyani et al., 2015).  
 331 The inertial range with a scaling exponent of  $-5/3$  is also denoted, however, there seems  
 332 to be a rather direct transition from the  $1/f$  region to a steeper slope with a scaling ex-  
 333 ponent of  $-8/3$ , which is consistent to previous studies like Czaykowska et al. (2001), Alexandrova  
 334 (2008), Chhiber et al. (2018), Macek et al. (2018). The steepening occurs at about four  
 335 times the ion gyro radius  $4 \cdot \rho_i \sim 500 \text{ km}$  (Note:  $d_i = 38 \text{ km}$  and  $\rho_i = 122 \text{ km}$ , so  
 336  $d_i + \rho_i = 160 \text{ km}$  which means that the steepening occurs at about three times ( $d_i +$   
 337  $\rho_i$ )).

338 The six symbols in Fig.5 denote structure functions of the six unique two-spacecraft  
 339 pairs. The pairing "14" for instance means the spatial separation from MMS1 to MMS4,  
 340 the others are "12", "13", "23", "34", "24". It is important to note that the often used  
 341 term "spatial lag" actually describes the spatial separation between the spacecraft av-  
 342 eraged over the time interval. Moreover, the analysis of MMS1 data is representative for

**Figure 4.** Mean positions of the four MMS spacecraft on February 26<sup>th</sup>, 2019: 15:00-15:40 in GSE coordinates. (a): XY-plane, (b): XZ-plane, (c): YZ-plane. The mean magnetic field direction  $\vec{B}_0$  (black) and the mean flow direction  $\mathbf{V}_{SW}$  (red) are scaled up for visualisation.

the other spacecraft as the variations between the different single-spacecraft structure functions are negligible.

It can be seen that the power of increments of the parallel (compressive) component of the magnetic field is higher than the power of the perpendicular components (see Fig. 5, panel (a)). Moreover, it is evident that there is in general a good agreement between the power of the multi-spacecraft measurements and the time-lagged measurements. However, it is important to note that the time-lagged measurements are obtained in flow direction, whereas the spatial-lagged measurements are taken in spacecraft baseline direction. This directional difference of the increments can be used to investigate the anisotropy by looking at the difference of the structure functions. The ratio of the spatial-lagged and nearest neighbor time-lagged measurement can be seen in panel (b) of Fig. 5. They are in general close to unity in the range of inter-spacecraft separations of 132 km to 916 km, or in units of the ion inertial length  $3.5 d_i$  to  $24 d_i$ . Nevertheless, the multi-spacecraft measurements show a consistently higher power than the single-spacecraft measurements ( $D_{\text{single}}/D_{\text{multi}} < 1$ ). Additionally, there seems to be a trend of increasingly smaller ratios for smaller and smaller lags. As the time-lagged structure functions indicate fluctuations in a different direction than the spatially-lagged structure functions, this enhanced derivation from 1 suggests higher anisotropy at smaller scales.

The equivalent spectrum for the derived electron plasma density can be seen in Fig. 5 panel (c). The electron density fluctuations represent the compressive part directly and can therefore quantitatively be compared with the compressive fluctuations of the magnetic field. In general, the scaling observed for the electron density is very similar in comparison with the magnetic field analysis. Only at large scales, the electron density equivalent spectrum seems to be steeper by a few percent. Additionally, there is good agreement between the power of the multi-spacecraft measurements. This can be checked by looking at the ratio of the structure functions plotted in panel (d). A trend of increasingly smaller ratios for smaller and smaller lags that seen in the magnetic field analysis cannot be observed clearly here.

## 4 Discussion

The electron plasma density derivation scheme (Andriopoulou et al., 2015; Andriopoulou et al., 2016; Andriopoulou et al., 2018; Torkar et al., 2019) is applied to a magnetopause crossing an magnetosheath interval on Feb. 26, 13:00-17:00 UT. The results are validated with MMS FPI measurements. The derived density data showed only a few percent difference to the interpolated plasma measurements. The methods enabled to obtain densities at much higher time resolution for the magnetosheath interval on Feb. 26, 2019, from 14:00 to 17:00 UT. There seems to be a trend of an underestimation of the electron density in the last two hours of the time interval of about 9 % on average, which may be due to assuming an average electron temperature  $T_e = 33$  eV within the total magnetosheath period.

The short interval with the dip of the ASPOC ion current of one emitter on MMS1 of max. 20 % from 16:15-16:25 UT (see Fig. 1) does not have any notable influence on the density derivation, since the ambient electron current dominates over the total ASPOC ion current for this particular interval. One may, however, need to more carefully select the interval with a stable ASPOC beam for other sparse plasma regions when applying this method.

We found that even if assuming that the MMS probes are in a very similar plasma environment, an average photoelectron curve modelled from one spacecraft cannot be used for density derivations on other MMS spacecraft without significant deviations from the FPI measurements (Andriopoulou et al., 2018). Hence, an average photoelectron curve was computed for each of the MMS spacecraft for the whole time interval from 13:00 UTC

**Figure 5.** Statistical analysis: Second-order ( $p=2$ ) structure functions of the mean magnetic field components and combined trace magnetic field (normalized, panel (a)) and electron density (panel c) as equivalent spectrum  $S^{(2)}$ . The X-Axis is units of the inverse spatial lag  $\lambda$  and is called effective wave number  $k^*$  ( $k^*$  is not identical to the wave number  $k$  of the regular frequency spectrum). Graphs denote MMS1 single spacecraft (time-lag) and symbols the multi-spacecraft (spatial-lag) structure functions (six different MMS combinations denoted by numbers in the legend).  $d_i$  is the ion inertial length and  $\rho_i$  the ion gyro radius. Three spectral slopes at the scaling exponents of -1, -5/3 and -8/3 are plotted in grey as a reference. Panels (b) and (d) show the ratios of structure functions of the trace magnetic field and electron density from single and multi-spacecraft measurements. The ratio is obtained using the spatial lag measurement and the nearest neighbor time-lagged measurement that is converted into a spatial lag  $\lambda$  using the ion bulk velocity.

393 to 17:00 UTC, 26<sup>th</sup> of February 2019. Including also the transition region from magne-  
 394 topause to magnetosheath (right before 14:00) enabled to have a larger range of poten-  
 395 tial values from 1.9 V to 5.8 V.

396 For the statistical analysis we selected a time interval that is long enough to make  
 397 higher-order statistics reasonable and when the magnetic field direction was rather sta-  
 398 ble to obtain a well defined mean field. Although finding such an interval in the mag-  
 399 netosheath was challenging we could select a 40 min time interval that had sufficient mea-  
 400 surement data of both, the magnetic field and the electron density to compute structure  
 401 functions of order two. While the equivalent spectrum for the electron density is slightly  
 402 steeper at large scales ( $k^* < 10^{-3} \text{ km}^{-1}$ ), both equivalent spectra displayed in panels  
 403 (a) and (c) in Fig. 5 show similar scaling laws. It can be observed that there is only a  
 404 short or even no inertial range (-5/3 slope), instead there is a direct transition from the  
 405 (1/f) range to the steeper (-8/3) region. This is consistent with findings of studies done  
 406 by Chasapis et al. (2017), Chhiber et al. (2018) and Roberts et al. (2020). The compres-  
 407 sive magnetic field component shows a consistently higher power than the transverse com-  
 408 ponents.

409 In previous studies employing multi-spacecraft measurements, like the ones men-  
 410 tioned above, the inter-spacecraft distances were much smaller for each spacecraft pair-  
 411 ing, and the constellation arranged in a tetrahedron. A comparison of time-lagged and  
 412 spatially-lagged was therefore limited to a small spatial range. In this study, the loga-  
 413 rithmic line constellation of the MMS spacecraft enabled comparison over almost one decade  
 414 in scale as demonstrated in Fig. 5. Nevertheless it is important to mention that it was  
 415 not accounted for the angle between the flow direction (time-lagged measurements) and  
 416 the spacecraft baselines (spatially-lagged measurements). To verify Taylor's Hypothe-  
 417 sis, meaning that the ratio of the structure functions is unity, the spacecraft baseline di-  
 418 rections and the flow direction need to be the same. Contrarily, if the goal is to find anisotropies,  
 419 these directions need to be different. In this case, however, it is not possible to fully ver-  
 420 ify Taylor's Hypothesis. Yet, the detail comparisons between the measurements over the  
 421 wide range of scales suggested some differences in the anisotropy.

422 The statistics of the electron density show in general very similar behavior in com-  
 423 parison to the magnetic field. Despite the fact that the derived electron density shows  
 424 good results in comparison to the FPI measurements one needs caution to compare point-  
 425 to-point derived density data of multiple spacecraft as noise and systematic errors might  
 426 be induced into the measurements. Further details on that issue can be found in Andriopoulou  
 427 et al. (2015).

## 428 5 Conclusions

429 Data obtained from the MMS Solar Wind Turbulence Campaign from February  
 430 26, 2019, provided a great data base to use density proxy data derived from the space-  
 431 craft potential for studying turbulence in the Earth's magnetosheath.

432 In this study we derive the electron density for each of the MMS satellites during  
 433 a period when the ASPOC instrument was operating and the spacecraft potential was  
 434 actively controlled. By also removing the spin tone in the spacecraft potential data, plasma  
 435 density with a much higher time resolution than the measurements from the MMS plasma  
 436 instruments (FPI) was derived. On average, the derived density is 3 % lower than the  
 437 FPI measurements in the relevant magnetosheath time interval, which means there is  
 438 a slight underestimation of the derived density. In future, the calibration method should  
 439 also be probed in intervals with lower plasma densities as the error tends to be higher  
 440 at lower densities. Moreover, in this study it was not possible, without increasing the  
 441 error substantially, to use a common photoelectron curve for the calibration of the data  
 442 of the four spacecraft although they were in a rather similar plasma environment and

not being separated more than 24.1 ion inertial lengths. This lack of commonality may be attributed to differences in the photoelectric properties between the spacecraft. Future studies could investigate the effect of including more currents in the current balance equation, depending on the environment of the spacecraft.

A 40 min time interval in the magnetosheath was chosen to validate the potential calibration and to study compressive turbulent fluctuations of the magnetic field and electron density. This analysis implied second-order structure functions expressed as equivalent spectra to examine spectral slopes. The finding that there is a direct transition from the  $(1/f)$  regime to the  $(-8/3)$  spectral slope with no inertial range ( $-5/3$  slope) in between is consistent with other studies, e.g., Chhiber et al. (2018). Analysis of magnetic field and electron density fluctuations suggests sub-ion scale intermittency in the magnetosheath. The intermittency is a sign for coherent structures that contribute to heating and dissipation in the magnetosheath (Osman et al., 2012; Wu et al., 2013). The magnetic field was transformed into mean-field coordinates, and it can be seen that the power of the structure-function of the parallel, compressive field component is higher than the transverse components, suggesting more intermittency.

A comparison of single- and multi-spacecraft statistics assuming the Taylor frozen-in approximation is made. There seems to be a better agreement between single and multi-spacecraft magnetic field data at large scales than an smaller ones. This suggests higher anisotropies at smaller scales. Nevertheless, it is unclear whether such anisotropies can be found by comparing single- and multi-spacecraft electron density data. More studies in the magnetosheath using multi-spacecraft data should be conducted, potentially using spacecraft potential calibration methods to obtain high-resolution plasma data and investigate turbulent fluctuations down to the smallest scales. Multi-spacecraft data are, however, not only important when examining increments and structure functions like in this paper or Chhiber et al. (2018), but also for other methods. Such include the wave telescope technique (Narita et al., 2022) or two spacecraft correlations (Osman & Horbury, 2007) for instance.

## Acknowledgments

All the MMS data is available at the MMS Science Data Center at the Laboratory for Atmospheric and Space Physics (LASP) at the University of Colorado, Boulder (<https://lasp.colorado.edu/mms/sdc/public/>). We want to thank all the MMS instrument teams as well as the SDC team for providing the already processed measurement data. Thank you also for the work done by the SPEDAS team in enabling easy access and plotting methods for the MMS data. This work was supported by the Austrian Research Promotion Agency (FFG): 873685.

## References

- Alexandrova, O. (2008, February). Solar wind vs magnetosheath turbulence and Alfvén vortices. *Nonlinear Processes in Geophysics*, *15*(1), 95-108. doi: 10.5194/npg-15-95-2008
- Andriopoulou, M., Nakamura, R., Torkar, K., Baumjohann, W., & Hoelzl, B. (2015). Deriving plasma densities in tenuous plasma regions, with the spacecraft potential under active control. *Journal of Geophysical Research: Space Physics*, *120*(11), 9594–9616.
- Andriopoulou, M., Nakamura, R., Torkar, K., Baumjohann, W., Torbert, R. B., Lindqvist, P. A., ... Russell, C. T. (2016, May). Study of the spacecraft potential under active control and plasma density estimates during the MMS commissioning phase. *Geophysical Research Letters*, *43*(10), 4858-4864. doi: 10.1002/2016GL068529
- Andriopoulou, M., Nakamura, R., Wellenzohn, S., Torkar, K., Baumjohann, W., Tor-

- bert, R. B., . . . Burch, J. L. (2018). Plasma density estimates from spacecraft potential using mms observations in the dayside magnetosphere. *Journal of Geophysical Research: Space Physics*, *123*(4), 2620–2629.
- Baker, D., Riesberg, L., Pankratz, C., Panneton, R., Giles, B., Wilder, F., & Ergun, R. (2016). Magnetospheric multiscale instrument suite operations and data system. *Space Science Reviews*, *199*(1-4), 545–575.
- Balcon, N., Payan, D., Belhaj, M., Tondou, T., & Inguibert, V. (2011). Secondary electron emission on space materials: Evaluation of the total secondary electron yield from surface potential measurements. *IEEE Transactions on Plasma Science*, *40*(2), 282–290.
- Bandyopadhyay, R., Matthaeus, W. H., Chasapis, A., Russell, C. T., Strangeway, R. J., Torbert, R. B., . . . Burch, J. L. (2020). Direct measurement of the solar-wind taylor microscale using mms turbulence campaign data. *The Astrophysical Journal*, *899*(1), 63.
- Borovsky, J. E., & Gary, S. P. (2014, July). How important are the alpha-proton relative drift and the electron heat flux for the proton heating of the solar wind in the inner heliosphere? *Journal of Geophysical Research (Space Physics)*, *119*(7), 5210-5219. doi: 10.1002/2014JA019758
- Bruno, R. (2019, May). Intermittency in Solar Wind Turbulence From Fluid to Kinetic Scales. *Earth and Space Science*, *6*(5), 656-672. doi: 10.1029/2018EA000535
- Bruno, R., & Carbone, V. (2013, May). The Solar Wind as a Turbulence Laboratory. *Living Reviews in Solar Physics*, *10*(1), 2. doi: 10.12942/lrsp-2013-2
- Burch, J., Moore, T., Torbert, R., & Giles, B. (2016). Magnetospheric multiscale overview and science objectives. *Space Science Reviews*, *199*(1-4), 5–21.
- Chasapis, A., Matthaeus, W. H., Bandyopadhyay, R., Chhiber, R., Ahmadi, N., Ergun, R. E., . . . Burch, J. L. (2020, 11). Scaling and anisotropy of solar wind turbulence at kinetic scales during the MMS turbulence campaign. *The Astrophysical Journal*, *903*(2), 127. Retrieved from <https://doi.org/10.3847/1538-4357/abb948> doi: 10.3847/1538-4357/abb948
- Chasapis, A., Matthaeus, W. H., Parashar, T. N., Le Contel, O., Retinò, A., Breuillard, H., . . . Saito, Y. (2017, February). Electron Heating at Kinetic Scales in Magnetosheath Turbulence. *The Astrophysical Journal*, *836*(2), 247. doi: 10.3847/1538-4357/836/2/247
- Chhiber, R., Chasapis, A., Bandyopadhyay, R., Parashar, T. N., Matthaeus, W. H., Maruca, B. A., . . . Gershman, D. J. (2018, December). Higher-Order Turbulence Statistics in the Earth’s Magnetosheath and the Solar Wind Using Magnetospheric Multiscale Observations. *Journal of Geophysical Research (Space Physics)*, *123*(12), 9941-9954. doi: 10.1029/2018JA025768
- Czaykowska, A., Bauer, T., Treumann, R., & Baumjohann, W. (2001). Magnetic field fluctuations across the earth’s bow shock. In *Annales geophysicae* (Vol. 19, pp. 275–287).
- Dudok de Wit, T., Alexandrova, O., Furno, I., Sorriso-Valvo, L., & Zimbardo, G. (2013, October). Methods for Characterising Microphysical Processes in Plasmas. *Space Science Reviews*, *178*(2-4), 665-693. doi: 10.1007/s11214-013-9974-9
- Fränzl, M., & Harper, D. (2002). Heliospheric coordinate systems. *Planetary and Space Science*, *50*(2), 217–233.
- Frisch, U. (1995). *Turbulence. The legacy of A.N. Kolmogorov*.
- Garner, R. (2019, 3). *Discovering Bonus Science With NASA’s Magnetospheric Multiscale Spacecraft*. <https://www.nasa.gov/feature/goddard/2019/discovering-bonus-science-with-nasa-s-magnetospheric-multiscale-spacecraft>. (Accessed: 2021-04-09)
- Graham, D. B., Vaivads, A., Khotyaintsev, Y. V., Eriksson, A. I., André, M., Malaspina, D. M., . . . Plaschke, F. (2018, September). Enhanced Escape

- 548 of Spacecraft Photoelectrons Caused by Langmuir and Upper Hybrid Waves.  
 549 *Journal of Geophysical Research (Space Physics)*, 123(9), 7534-7553. doi:  
 550 10.1029/2018JA025874
- 551 Kiyani, K., Chapman, S. C., & Hnat, B. (2006, 11). Extracting the scaling ex-  
 552 ponents of a self-affine, non-gaussian process from a finite-length time series.  
 553 *Phys. Rev. E*, 74, 051122. Retrieved from [https://link.aps.org/doi/](https://link.aps.org/doi/10.1103/PhysRevE.74.051122)  
 554 [10.1103/PhysRevE.74.051122](https://link.aps.org/doi/10.1103/PhysRevE.74.051122) doi: 10.1103/PhysRevE.74.051122
- 555 Kiyani, K. H., Osman, K. T., & Chapman, S. C. (2015). *Dissipation and heating in*  
 556 *solar wind turbulence: from the macro to the micro and back again*. The Royal  
 557 Society Publishing.
- 558 Klein, K. G., Alexandrova, O., Bookbinder, J., Caprioli, D., Case, A. W., Chandran,  
 559 B. D. G., ... Whittlesey, P. (2019, March). [Plasma 2020 Decadal] Multi-  
 560 point Measurements of the Solar Wind: A Proposed Advance for Studying  
 561 Magnetized Turbulence. *arXiv e-prints*, arXiv:1903.05740.
- 562 Kolmogorov, A. (1941, January). The Local Structure of Turbulence in Incompress-  
 563 ible Viscous Fluid for Very Large Reynolds' Numbers. *Akademiia Nauk SSSR*  
 564 *Doklady*, 30, 301-305.
- 565 Lindqvist, P. A., Olsson, G., Torbert, R. B., King, B., Granoff, M., Rau, D., ...  
 566 Tucker, S. (2016, March). The Spin-Plane Double Probe Electric Field  
 567 Instrument for MMS. *Space Science Reviews*, 199(1-4), 137-165. doi:  
 568 10.1007/s11214-014-0116-9
- 569 Macek, W. M., Krasnińska, A., Silveira, M. V. D., Sibeck, D. G., Wawrzaszek, A.,  
 570 Burch, J. L., & Russell, C. T. (2018, September). Magnetospheric Multiscale  
 571 Observations of Turbulence in the Magnetosheath on Kinetic Scales. *The*  
 572 *Astrophysical Journal Letters*, 864(2), L29. doi: 10.3847/2041-8213/aad9a8
- 573 Markwardt, C. B. (2009). Non-linear least squares fitting in idl with mpfit. *arXiv*  
 574 *preprint arXiv:0902.2850*.
- 575 Matthaeus, W. H., Dasso, S., Weygand, J. M., Milano, L. J., Smith, C. W., &  
 576 Kivelson, M. G. (2005, 12). Spatial correlation of solar-wind turbulence  
 577 from two-point measurements. *Phys. Rev. Lett.*, 95, 231101. Retrieved  
 578 from <https://link.aps.org/doi/10.1103/PhysRevLett.95.231101> doi:  
 579 10.1103/PhysRevLett.95.231101
- 580 Matthaeus, W. H., Wan, M., Servidio, S., Greco, A., Osman, K. T., Oughton, S., &  
 581 Dmitruk, P. (2015, April). Intermittency, nonlinear dynamics and dissipation  
 582 in the solar wind and astrophysical plasmas. *Philosophical Transactions of*  
 583 *the Royal Society of London Series A*, 373(2041), 20140154-20140154. doi:  
 584 10.1098/rsta.2014.0154
- 585 Mott-Smith, H. M., & Langmuir, I. (1926). The theory of collectors in gaseous dis-  
 586 charges. *Physical review*, 28(4), 727.
- 587 Nakagawa, T., Ishii, T., Tsuruda, K., Hayakawa, H., & Mukai, T. (2000, April). Net  
 588 current density of photoelectrons emitted from the surface of the GEOTAIL  
 589 spacecraft. *Earth, Planets and Space*, 52, 283-292. doi: 10.1186/BF03351637
- 590 Nakamura, R., Torkar, K., Andriopoulou, M., Jeszenszky, H., Escoubet, C., Cipriani,  
 591 F., ... others (2017). Initial results from the active spacecraft potential control  
 592 onboard magnetospheric multiscale mission. *IEEE Transactions on Plasma*  
 593 *Science*, 45(8), 1847-1852.
- 594 Narita, Y., Gary, S. P., Saito, S., Glassmeier, K.-H., & Motschmann, U. (2011).  
 595 Dispersion relation analysis of solar wind turbulence. *Geophysical Research*  
 596 *Letters*, 38(5). Retrieved from [https://agupubs.onlinelibrary.wiley](https://agupubs.onlinelibrary.wiley.com/doi/abs/10.1029/2010GL046588)  
 597 [.com/doi/abs/10.1029/2010GL046588](https://agupubs.onlinelibrary.wiley.com/doi/abs/10.1029/2010GL046588) doi: [https://doi.org/10.1029/](https://doi.org/10.1029/2010GL046588)  
 598 [2010GL046588](https://doi.org/10.1029/2010GL046588)
- 599 Narita, Y., Glassmeier, K. H., & Motschmann, U. (2022, February). The Wave  
 600 Telescope Technique. *Journal of Geophysical Research (Space Physics)*, 127(2),  
 601 e30165. doi: 10.1029/2021JA030165
- 602 Osman, K. T., & Horbury, T. S. (2007, January). Multispacecraft Measurement of

- 603 Anisotropic Correlation Functions in Solar Wind Turbulence. *The Astrophysical*  
 604 *Journal*, 654(1), L103-L106. doi: 10.1086/510906
- 605 Osman, K. T., Matthaeus, W. H., Wan, M., & Rappazzo, A. F. (2012, 6). Intermit-  
 606 tency and local heating in the solar wind. *Phys. Rev. Lett.*, 108, 261102. Re-  
 607 trieved from <https://link.aps.org/doi/10.1103/PhysRevLett.108.261102>  
 608 doi: 10.1103/PhysRevLett.108.261102
- 609 Oughton, S., & Matthaeus, W. H. (2020, July). Critical Balance and the Physics  
 610 of Magnetohydrodynamic Turbulence. *The Astrophysical Journal*, 897(1), 37.  
 611 doi: 10.3847/1538-4357/ab8f2a
- 612 Oughton, S., Matthaeus, W. H., Wan, M., & Osman, K. T. (2015). Anisotropy in  
 613 solar wind plasma turbulence. *Philosophical Transactions of the Royal Society*  
 614 *A: Mathematical, Physical and Engineering Sciences*, 373(2041), 20140152.  
 615 Retrieved from [https://royalsocietypublishing.org/doi/abs/10.1098/](https://royalsocietypublishing.org/doi/abs/10.1098/rsta.2014.0152)  
 616 [rsta.2014.0152](https://royalsocietypublishing.org/doi/abs/10.1098/rsta.2014.0152) doi: 10.1098/rsta.2014.0152
- 617 Pedersen, A. (1995). Solar wind and magnetosphere plasma diagnostics by space-  
 618 craft electrostatic potential measurements. In *Annales geophysicae* (Vol. 13,  
 619 pp. 118–129).
- 620 Pedersen, A., Cattell, C. A., Fälthammar, C. G., Formisano, V., Lindqvist, P. A.,  
 621 Mozer, F., & Torbert, R. (1984, March). Quasistatic electric field measure-  
 622 ments with spherical double probes on the GEOS and ISEE satellites. *Space*  
 623 *Science Reviews*, 37(3-4), 269-312. doi: 10.1007/BF00226365
- 624 Pedersen, A., Décréau, P., Escoubet, C. P., Gustafsson, G., Laakso, H., Lindqvist,  
 625 P. A., ... Vaivads, A. (2001, October). Four-point high time resolu-  
 626 tion information on electron densities by the electric field experiments  
 627 (EFW) on Cluster. *Annales Geophysicae*, 19(10), 1483-1489. doi:  
 628 10.5194/angeo-19-1483-2001
- 629 Pedersen, A., Lybekk, B., André, M., Eriksson, A., Masson, A., Mozer, F. S.,  
 630 ... Whipple, E. (2008, July). Electron density estimations derived from  
 631 spacecraft potential measurements on Cluster in tenuous plasma regions.  
 632 *Journal of Geophysical Research (Space Physics)*, 113(A7), A07S33. doi:  
 633 10.1029/2007JA012636
- 634 Perrone, D., Stansby, D., Horbury, T. S., & Matteini, L. (2019, March). Radial evo-  
 635 lution of the solar wind in pure high-speed streams: HELIOS revised observa-  
 636 tions. *Monthly Notices of the Royal Astronomical Society*, 483(3), 3730-3737.  
 637 doi: 10.1093/mnras/sty3348
- 638 Pollock, C., Moore, T., Jacques, A., Burch, J., Gliese, U., Saito, Y., ... others  
 639 (2016). Fast plasma investigation for magnetospheric multiscale. *Space Science*  
 640 *Reviews*, 199(1-4), 331–406.
- 641 Roberts, O. W., Alexandrova, O., Sorriso-Valvo, L., Vörös, Z., Nakamura, R., Fis-  
 642 cher, D., ... Yearby, K. (2022). Scale-dependent kurtosis of magnetic field  
 643 fluctuations in the solar wind: A multi-scale study with cluster 2003–2015.  
 644 *Journal of Geophysical Research: Space Physics*, 127(9), e2021JA029483.  
 645 Retrieved from [https://agupubs.onlinelibrary.wiley.com/doi/abs/](https://agupubs.onlinelibrary.wiley.com/doi/abs/10.1029/2021JA029483)  
 646 [10.1029/2021JA029483](https://agupubs.onlinelibrary.wiley.com/doi/abs/10.1029/2021JA029483) (e2021JA029483 2021JA029483) doi: [https://doi.org/](https://doi.org/10.1029/2021JA029483)  
 647 [10.1029/2021JA029483](https://doi.org/10.1029/2021JA029483)
- 648 Roberts, O. W., Li, X., & Jeska, L. (2015, 3). A STATISTICAL STUDY OF  
 649 THE SOLAR WIND TURBULENCE AT ION KINETIC SCALES USING  
 650 THEK-FILTERING TECHNIQUE AND CLUSTER DATA. *The Astrophysical*  
 651 *Journal*, 802(1), 2. Retrieved from [https://doi.org/10.1088/0004-637x/](https://doi.org/10.1088/0004-637x/802/1/2)  
 652 [802/1/2](https://doi.org/10.1088/0004-637x/802/1/2) doi: 10.1088/0004-637x/802/1/2
- 653 Roberts, O. W., Li, X., & Li, B. (2013, 5). KINETIC PLASMA TURBULENCE  
 654 IN THE FAST SOLAR WIND MEASURED BY CLUSTER. *The Astrophysical*  
 655 *Journal*, 769(1), 58. Retrieved from [https://doi.org/10.1088/0004-637x/](https://doi.org/10.1088/0004-637x/769/1/58)  
 656 [769/1/58](https://doi.org/10.1088/0004-637x/769/1/58) doi: 10.1088/0004-637x/769/1/58
- 657 Roberts, O. W., Nakamura, R., Torkar, K., Graham, D. B., Gershman, D. J.,

- 658 Holmes, J. C., ... Giles, B. L. (2020, September). Estimation of the Electron  
659 Density From Spacecraft Potential During High-Frequency Electric Field Fluc-  
660 tuations. *Journal of Geophysical Research (Space Physics)*, 125(9), e27854.  
661 doi: 10.1029/2020JA027854
- 662 Roberts, O. W., Nakamura, R., Torkar, K., Narita, Y., Holmes, J. C., Vörös, Z.,  
663 ... others (2020). Sub-ion scale compressive turbulence in the solar wind:  
664 Mms spacecraft potential observations. *The Astrophysical Journal Supplement*  
665 *Series*, 250(2), 35.
- 666 Roberts, O. W., Narita, Y., Li, X., Escoubet, C. P., & Laakso, H. (2017, July).  
667 Multipoint analysis of compressive fluctuations in the fast and slow solar wind.  
668 *Journal of Geophysical Research (Space Physics)*, 122(7), 6940-6963. doi:  
669 10.1002/2016JA023552
- 670 Russell, C. T., Anderson, B. J., Baumjohann, W., Bromund, K. R., Dearborn,  
671 D., Fischer, D., ... Richter, I. (2016, March). The Magnetospheric Mul-  
672 tiscala Magnetometers. *Space Science Reviews*, 199(1-4), 189-256. doi:  
673 10.1007/s11214-014-0057-3
- 674 Taylor, G. I. (1938). The spectrum of turbulence. *Proceedings of the Royal Society of*  
675 *London. Series A-Mathematical and Physical Sciences*, 164(919), 476-490.
- 676 Torkar, K., Nakamura, R., & Andriopoulou, M. (2015, September). Interdependen-  
677 cies Between the Actively Controlled Cluster Spacecraft Potential, Ambient  
678 Plasma, and Electric Field Measurements. *IEEE Transactions on Plasma*  
679 *Science*, 43(9), 3054-3063. doi: 10.1109/TPS.2015.2422733
- 680 Torkar, K., Nakamura, R., Andriopoulou, M., Giles, B. L., Jeszenszky, H.,  
681 Khotyaintsev, Y. V., ... Torbert, R. B. (2017, December). Influence of the  
682 Ambient Electric Field on Measurements of the Actively Controlled Spacecraft  
683 Potential by MMS. *Journal of Geophysical Research (Space Physics)*, 122(12),  
684 12,019-12,030. doi: 10.1002/2017JA024724
- 685 Torkar, K., Nakamura, R., Tajmar, M., Scharlemann, C., Jeszenszky, H., Laky, G.,  
686 ... Svenes, K. (2016). Active spacecraft potential control investigation. *Space*  
687 *Science Reviews*, 199(1-4), 515-544.
- 688 Torkar, K., Nakamura, R., Wellenzohn, S., Jeszenszky, H., Torbert, R. B., Lindqvist,  
689 P. A., ... Giles, B. L. (2019, August). Improved Determination of Plasma  
690 Density Based on Spacecraft Potential of the Magnetospheric Multiscale Mis-  
691 sion Under Active Potential Control. *IEEE Transactions on Plasma Science*,  
692 47(8), 3636-3647. doi: 10.1109/TPS.2019.2911425
- 693 Williams, L. L., Zank, G. P., & Matthaeus, W. H. (1995, September). Dissipa-  
694 tion of pickup-induced waves: A solar wind temperature increase in the outer  
695 heliosphere? *Journal of Geophysical Research*, 100(A9), 17059-17068. doi:  
696 10.1029/95JA01261
- 697 Wu, P., Perri, S., Osman, K., Wan, M., Matthaeus, W. H., Shay, M. A., ... Chap-  
698 man, S. (2013). Intermittent heating in solar wind and kinetic simulations.  
699 *The Astrophysical Journal*, 763(2), L30. Retrieved from [https://doi.org/](https://doi.org/10.1088/2041-8205/763/2/L30)  
700 [10.1088/2041-8205/763/2/L30](https://doi.org/10.1088/2041-8205/763/2/L30) doi: 10.1088/2041-8205/763/2/L30
- 701 Yao, S., He, J. S., Marsch, E., Tu, C. Y., Pedersen, A., Rème, H., & Trotignon,  
702 J. G. (2011, February). Multi-scale Anti-correlation Between Electron Density  
703 and Magnetic Field Strength in the Solar Wind. *The Astrophysical Journal*,  
704 728(2), 146. doi: 10.1088/0004-637X/728/2/146

**Figure 1.**

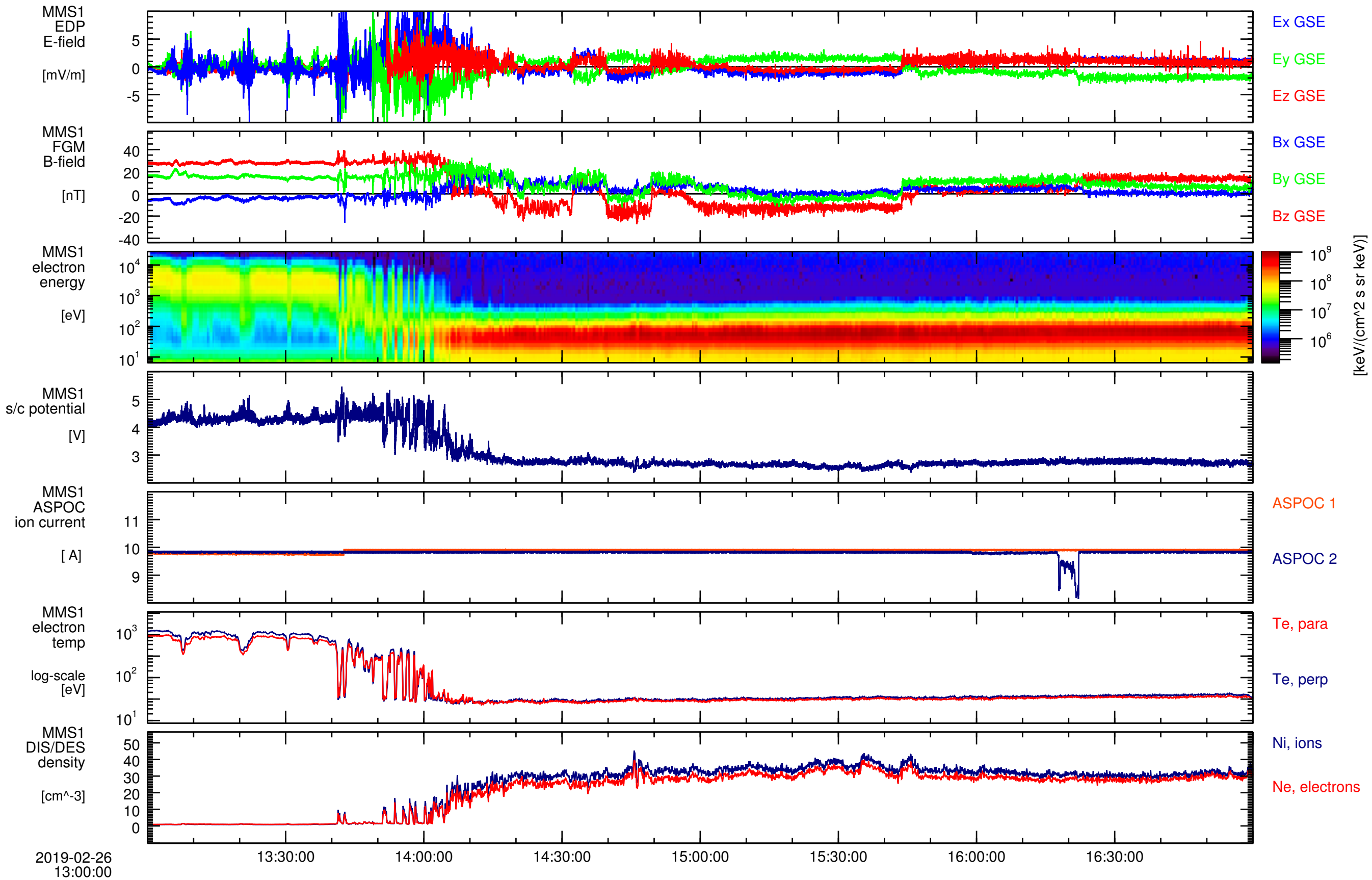


Figure 2.

MMS 1: 2019-02-26/13:00:00 to 2019-02-26/17:00:00: binned data

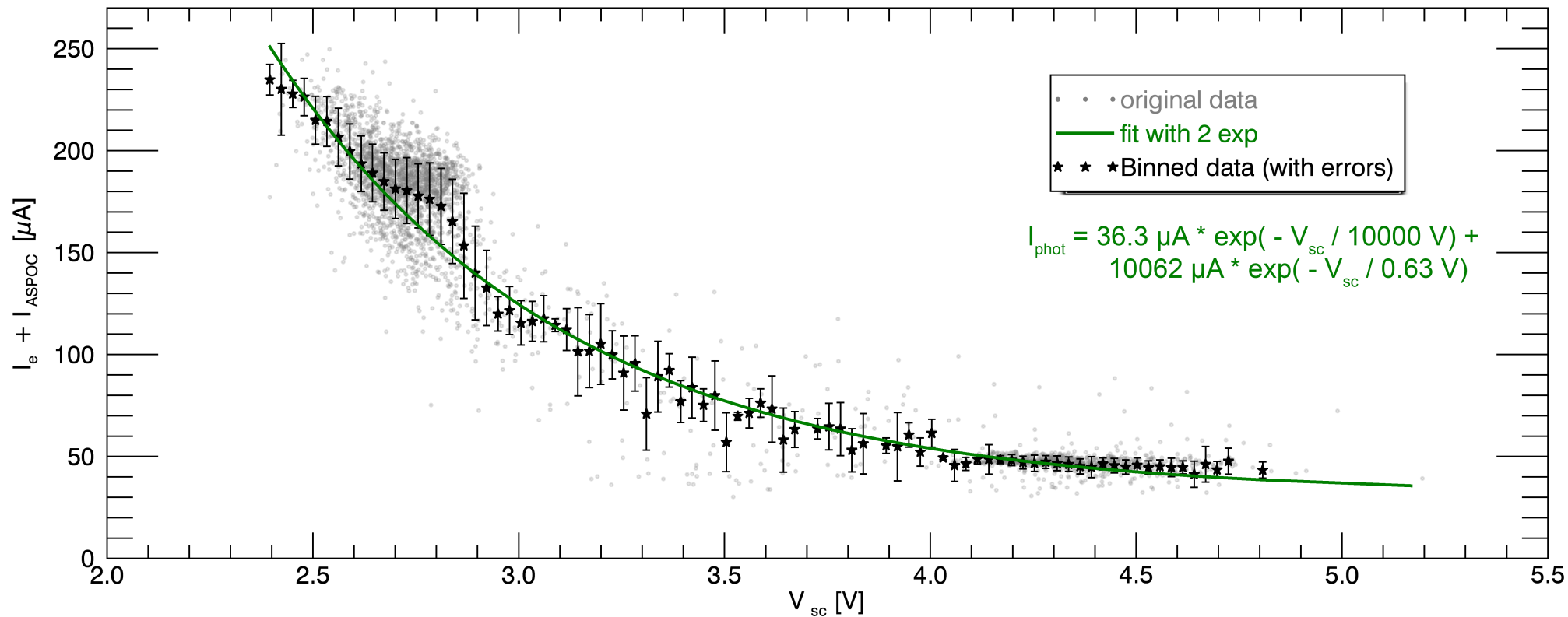


Figure 3.

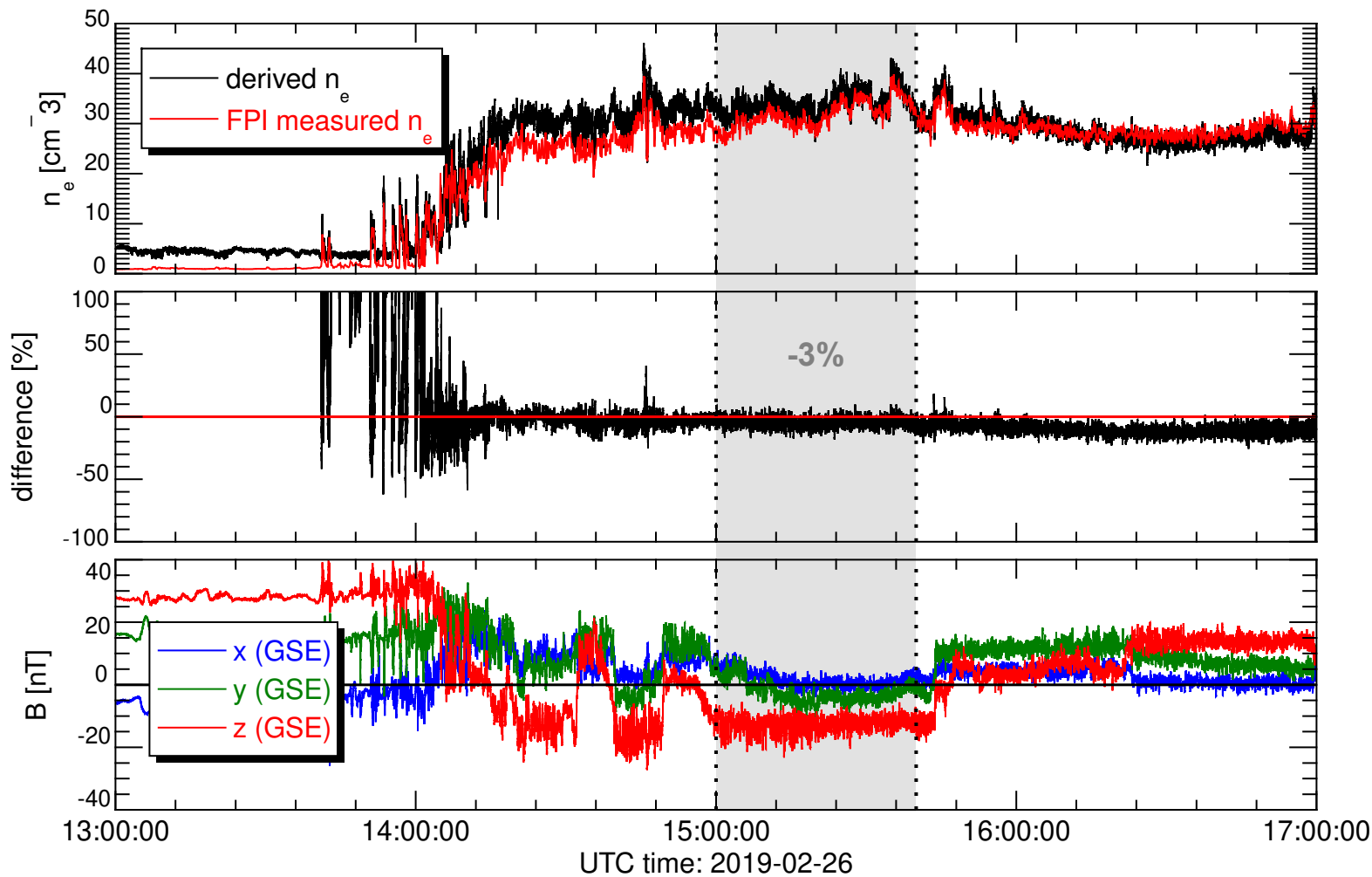
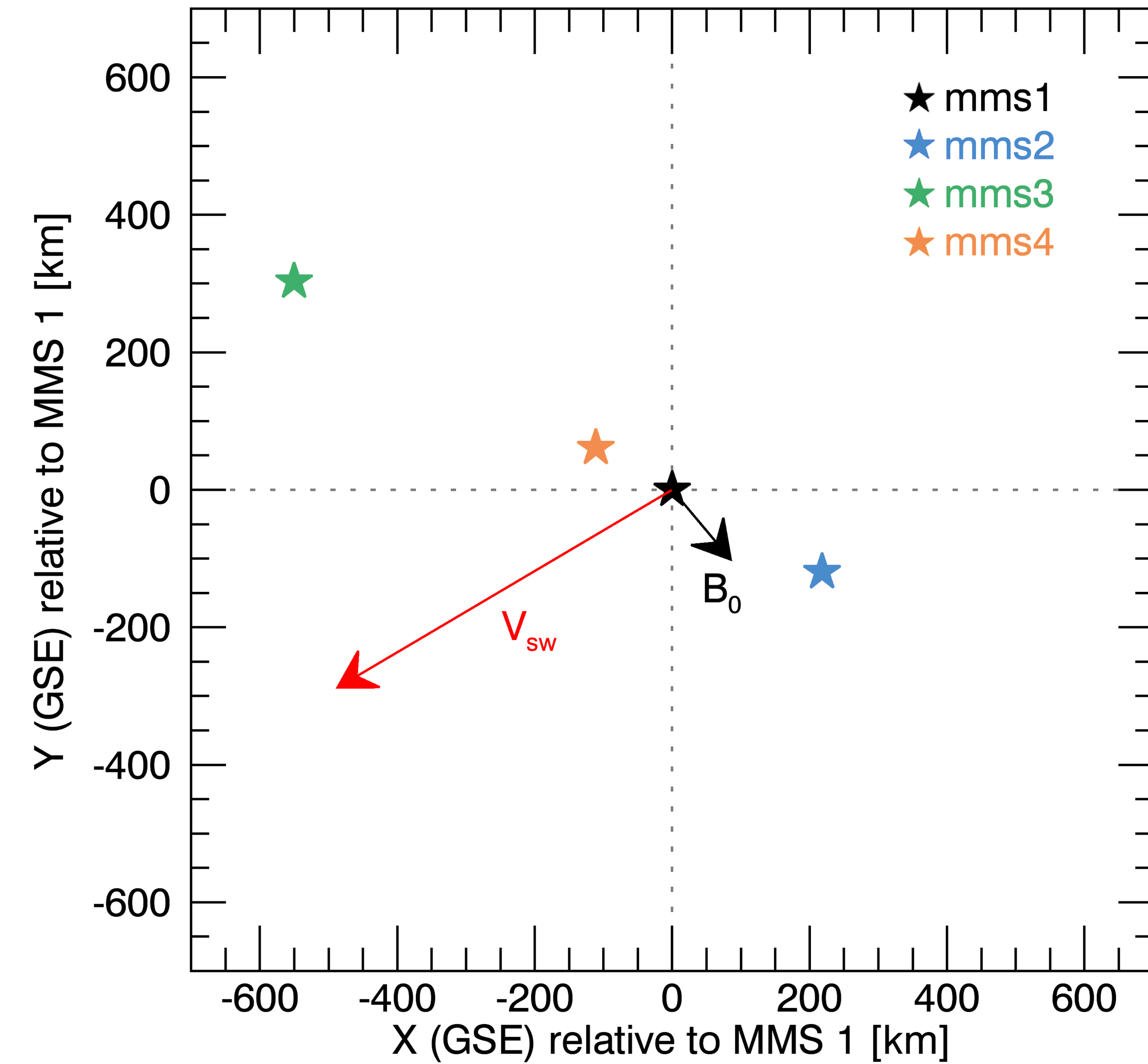
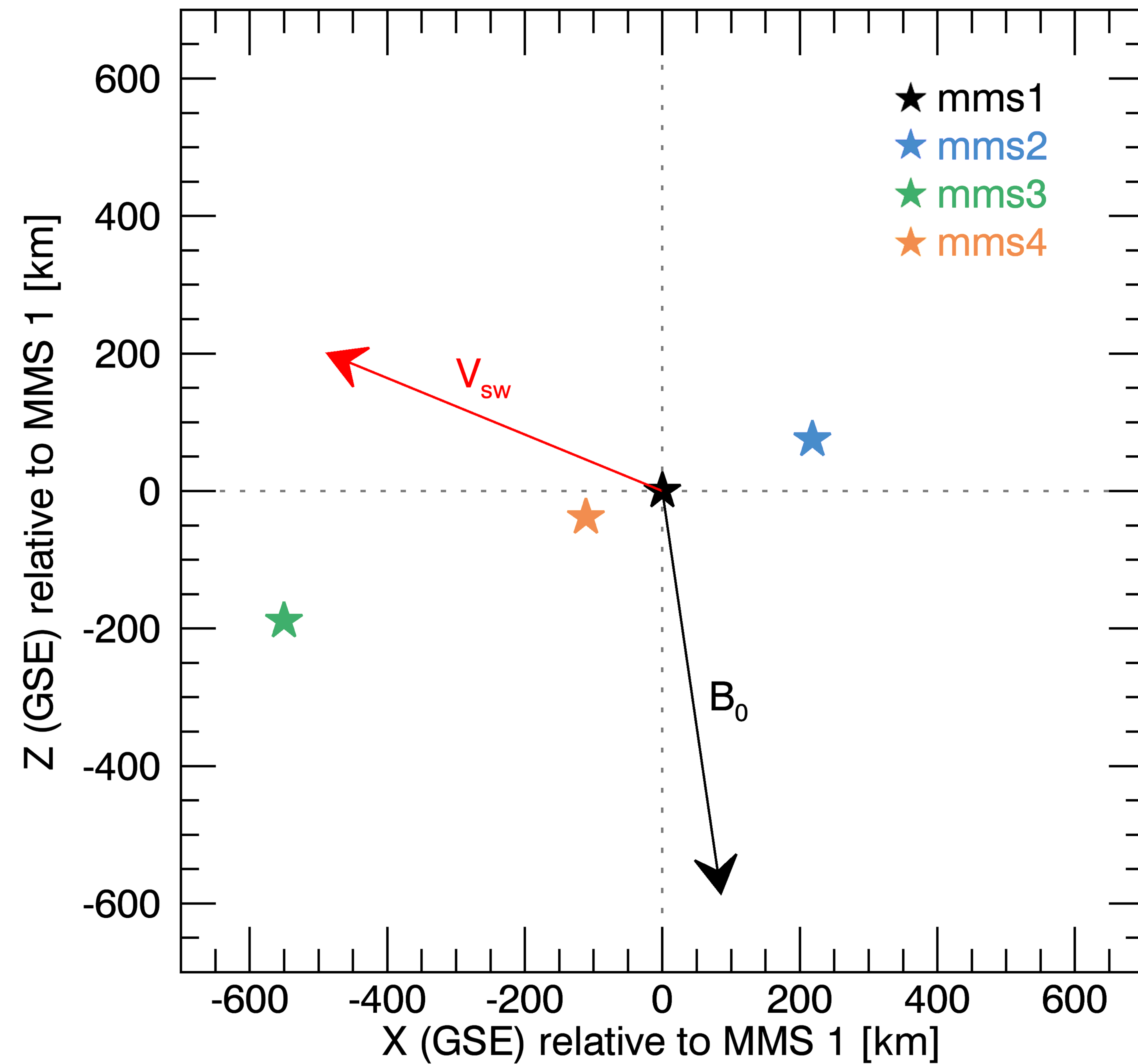


Figure 4.

(a)



(b)



(c)

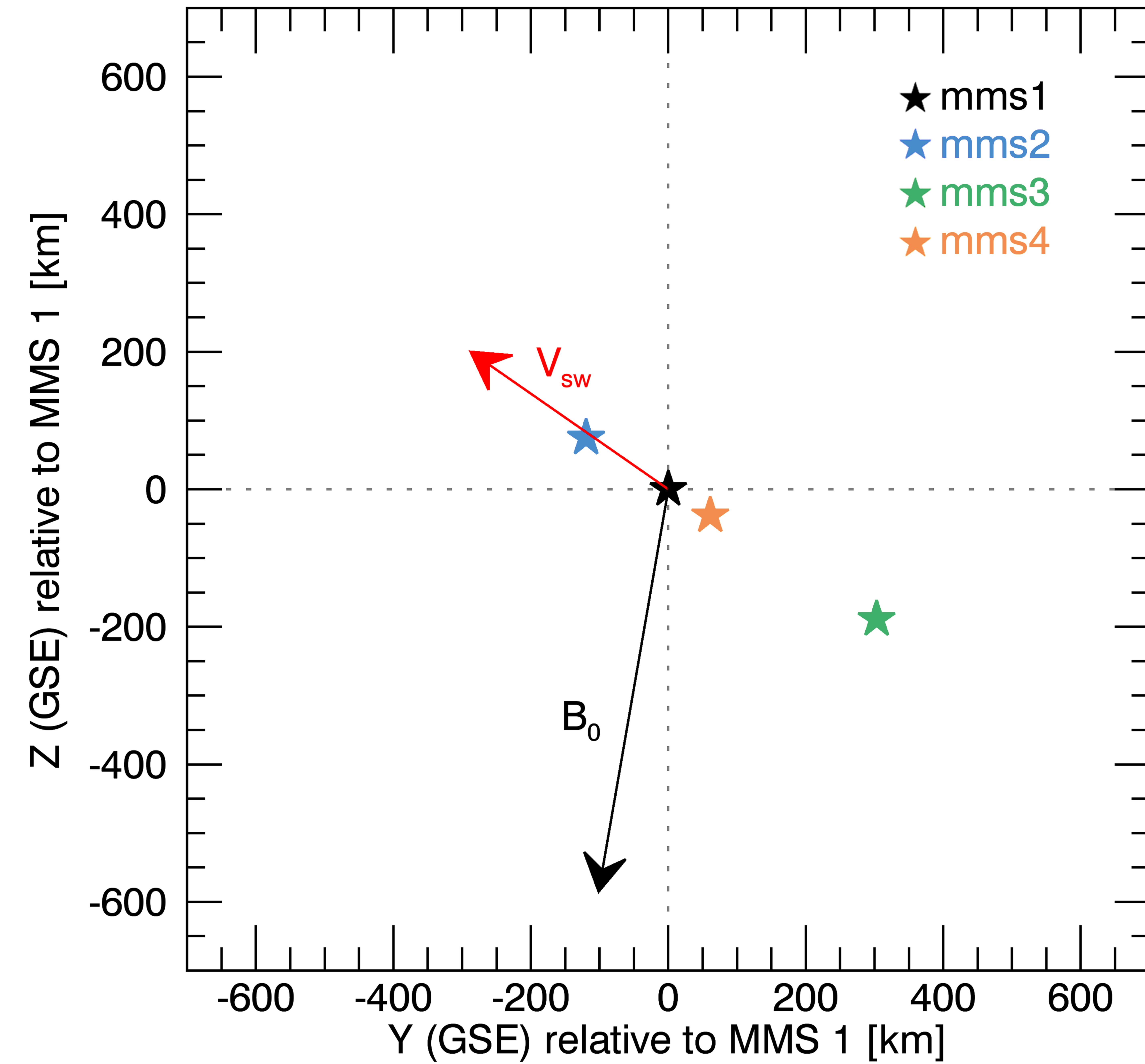
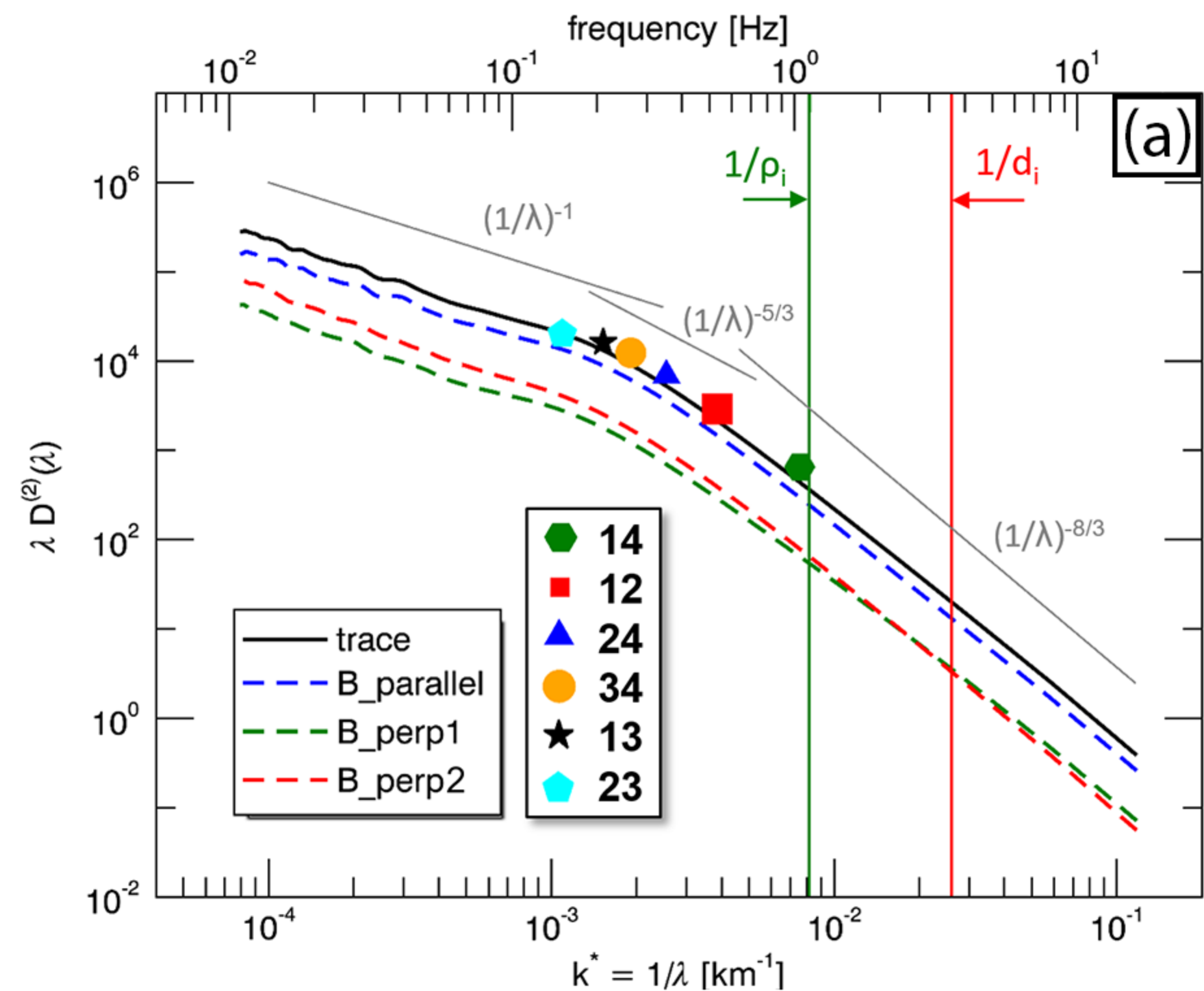
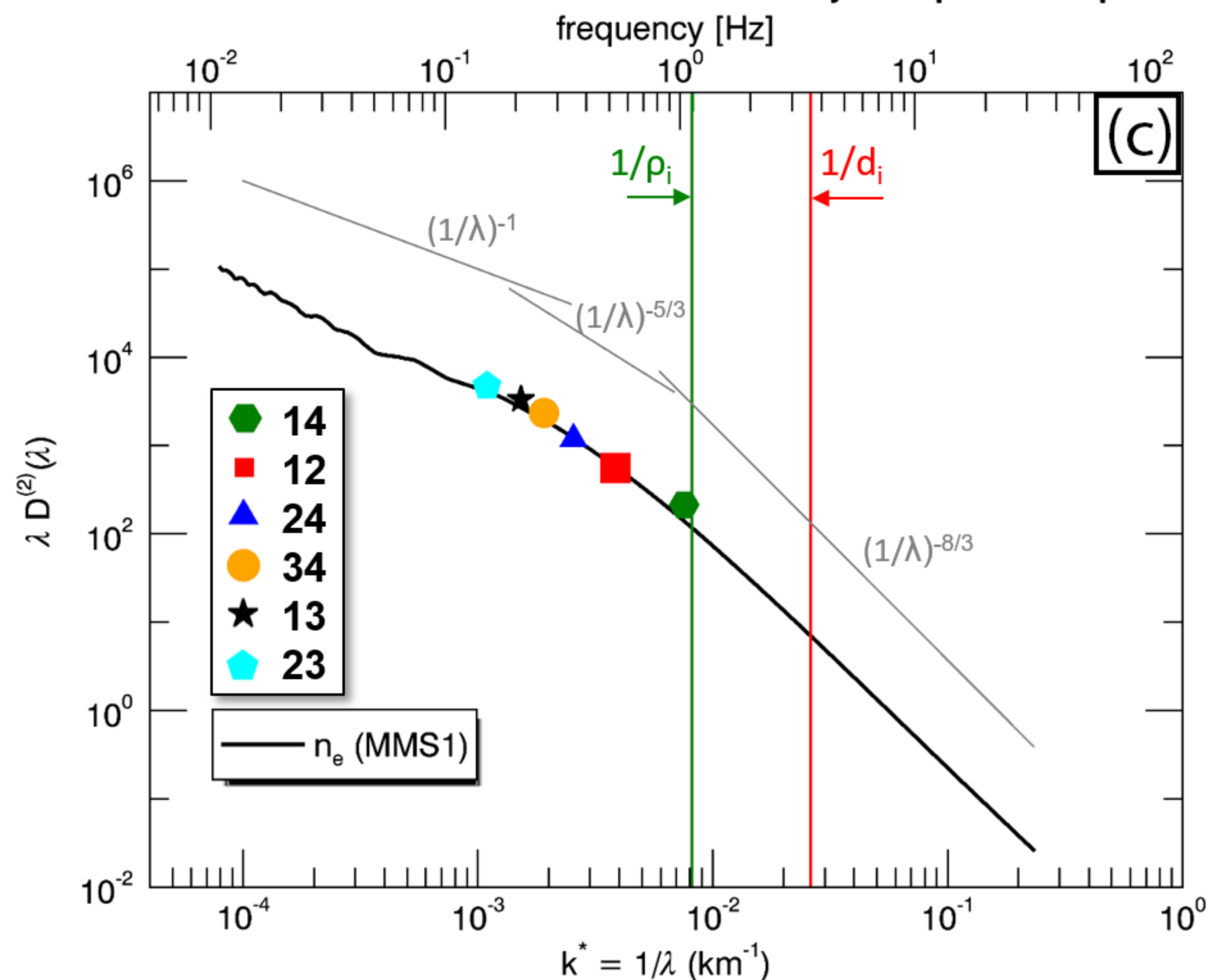


Figure 5.

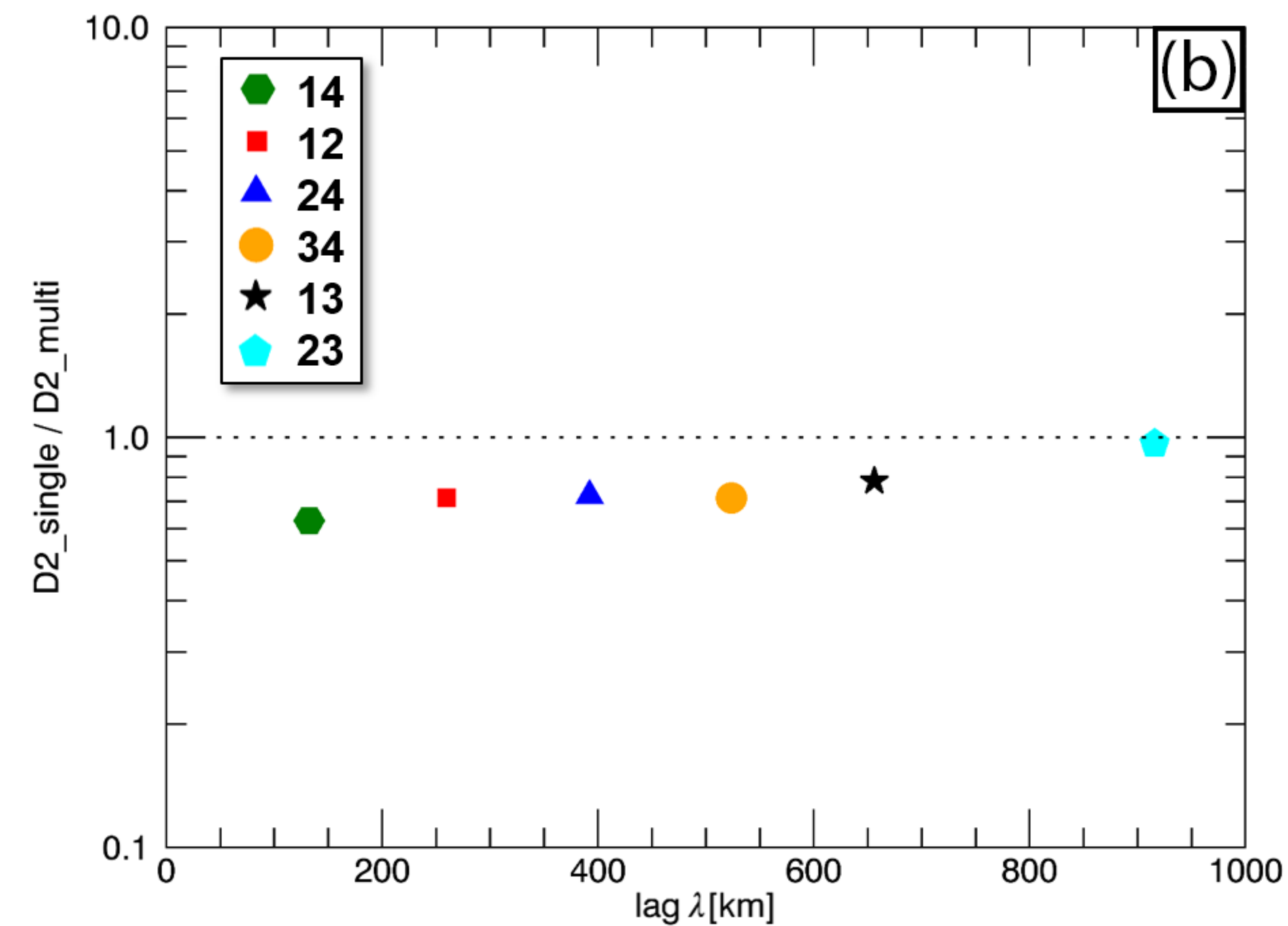
**Equivalent Spectrum of Trace Magnetic Field (MMS1)**



**2<sup>nd</sup>-order Structure Function of Electron Density as Equivalent Spectrum**



**2nd-order Structure Function Ratios (trace magnetic field; MMS1)**



**2nd-order Structure Function Ratios (electron density; MMS1)**

